ADVANCED FUNCTIONAL MATERIALS
www.afm-journal.de

Hierarchical Structuring in Block Copolymer Nanocomposites through Two Phase-Separation Processes Operating on Different Time Scales

Elina Ploshnik, Karol M. Langner, Amit Halevi, Meirav Ben-Lulu, Axel H. E. Müller, Johannes G. E. M. Fraaije, G. J. Agur Sevink, and Roy Shenhar**

Tailoring the size and surface chemistry of nanoparticles allows one to control their position in a block copolymer, but this is usually limited to one-dimensional distribution across domains. Here, the hierarchical assembly of poly(ethylene oxide)-stabilized gold nanoparticles (Au-PEO) into hexagonally packed clusters inside mesostructured ultrathin films of polystyrene-*block*-poly(methyl methacrylate) (PS-*b*-PMMA) is described. A close examination of the structural evolution at different nanoparticle filling fractions and PEO ligand molecular weights suggests that the mechanism leading to this structure-within-structure is the existence of two phase separation processes operating on different time scales. The length of the PEO ligand is shown to influence not only the interparticle distances but also the phase separation processes. These conclusions are supported by novel mesoscopic simulations, which provide additional insight into the kinetic and thermodynamic factors that are responsible for this behavior.

1. Introduction

The ability to assemble nanoparticles (NP) hierarchically, with control over their positioning and spacing, is considered an important step towards applications where collective properties are sensitive to the morphology of nanoparticle aggregates.[1–11] Using block copolymers (BCPs) as matrices to organize metal and semiconductor NPs through microphase separation has gained attention in recent years.[11–15] The main reason is that BCP nanocomposites offer flexibility in chemical design, due to the large variety of synthetically viable BCPs and the accessibility of a few useful morphologies such as alternating lamellae, hexagonally packed cylinders and cubically packed spheres.

Nanoparticles can be segregated selectively to one BCP domain by tailoring their surface chemistry to be compatible with the corresponding copolymer block.[16–30] This often leads to morphological transitions in the BCP phase due to an increased volume fraction of the hosting domain,[31–53] and may also result in bicontinuous morphologies.[43,48,52,54] Both experimental work[55–60] and simulations[25,43,61–65] suggest that the size of NPs, relative to the microdomain spacing, L_0, is important for their distribution. Namely, relatively small NPs tend to segregate to the interface between BCP domains, and large NPs sequester to the center of the hosting domain. This behavior is often explained by an enhanced decrease in the entropy of copolymer chains when they need to circumvent large NPs.[25,43,61–65] Other important factors for NP distribution include favorable ligand-polymer interactions (selectivity) and, in thin films, interfacial interactions at the free surface and substrate.[66–69] More complex systems provide additional possibilities, for example ternary BCP/homopolymer blends assembled over patterned substrates exhibit bimodal distributions of NPs around domain centers.[70]

The picture evolving from the current literature is one of increasing levels of control over the organization of NPs using BCPs, from mere selectivity of NPs toward specific block copolymer domains to some degree of control over the distribution of NPs inside domains. This is limited, however, to segregating nanoparticles to interfaces or around the centers of domains, and NP location is typically discussed in terms of a one-dimensional distribution across domains. Here, we proceed and demonstrate the formation of hierarchical BCP/NP composites, featuring hexagonal arrangements of NPs with controlled nearest neighbor distance inside one block copolymer domain. Such structures are obtained, in essence, by adding another dimension of chemical incompatibility to the thermodynamic system.

E. Ploshnik, A. Halevi, M. Ben-Lulu, Prof. R. Shenhar
The Institute of Chemistry and the Center for Nanoscience and Nanotechnology
The Hebrew University of Jerusalem
Jerusalem 91904, Israel
E-mail: roys@huji.ac.il

K. M. Langner, Prof. J. G. E. M. Fraaije, Dr. G. J. A. Sevink
Leiden Institute of Chemistry
Universiteit Leiden
P.O. Box 9502, 2300 RA Leiden, The Netherlands
E-mail: a.sevink@chem.leidenuniv.nl

Prof. A. H. E. Müller
Institute of Organic Chemistry
University of Mainz
Mainz, 55099, Germany

DOI: 10.1002/adfm.201300091

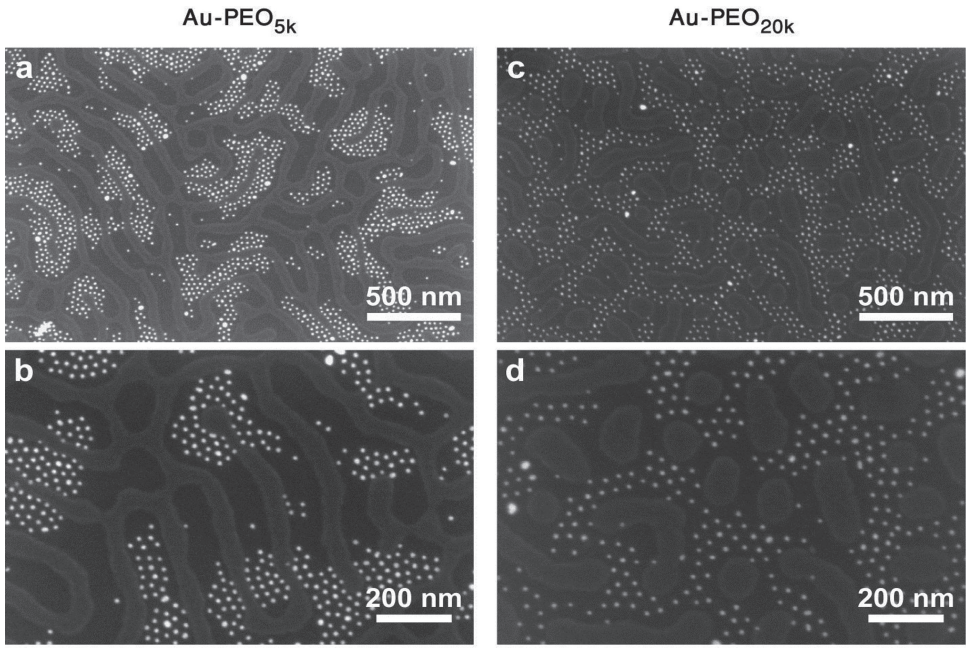

Figure 1. HR-SEM images, at two magnifications, of ultrathin PS-*b*-PMMA/Au-PEO films after 14 h of annealing in chloroform vapor, with different lengths of the PEO ligands: a,b) 5 kDa ($\sigma = 460 \pm 40$ NP μm^{-2}) and c,d) 20 kDa ($\sigma = 320 \pm 10$ NP μm^{-2}). Black and gray domains correspond to the PMMA and PS domains, respectively.

2. Results and Discussion

The majority of literature on BCP/NP assembly discusses the phase behavior of A-B block copolymers mixed with A-compatible NPs. Our approach is to explore the morphology of an A-B type BCP with NPs that are incompatible with both domains, but to different extents. We focus on a system consisting of a polystyrene-*block*-poly(methyl methacrylate) (PS-*b*-PMMA, $M_n = 1.0 \times 10^6$ Da, polydispersity index (PDI) = 1.2, 35 wt% PS, showing a lamellar morphology in a thin film; see Supporting Information Figure S1) and gold NPs coated with poly(ethylene oxide) (Au-PEO).[32] The lower incompatibility of PEO with PMMA than with PS[71,72] should lead to the segregation of NPs to PMMA domains.[73]

The Au-PEO NPs were synthesized by ligand exchange with PEO-SH ligands onto 13 nm citrate-stabilized gold cores (see Experimental Section). To investigate the effect of ligand size, two molecular weights of the PEO-SH ligand (M_n either 5000 or 20 000 Da, denoted as 5k or 20k for brevity) were used, resulting in an increase in the hydrodynamic radius to ca. 50 and 65 nm, respectively (see Supporting Information Table S1). The relatively low molecular weights of the PEO-SH ligands used compared to the high molecular weight of the PMMA block guarantees the suppression of PEO crystallinity (as will be shown below). The copolymer and the Au-PEO NPs were mixed in different ratios and spin-coated as ultrathin films on the order of the NP diameter (ca. 30 nm, much thinner than the long period of the BCP lamellar morphology, $L_0 = 150$ nm, as measured by AFM, see Experimental section and Supporting Information Figure S1). The severe reduction of the third dimension allows for an improved control over kinetic factors in thin film phenomena, including the formation of terraces and (de)wetting, and has the advantage that we may consider the hierarchical self-assembly as a quasi-two-dimensional process for all practical purposes (see discussion below). NP filling fractions were quantified by the resulting areal density, σ, which can be determined directly from image analysis, and fell in the range 200–1200 NP μm^{-2}.

Figure 1 shows high resolution scanning electron microscopy (HR-SEM) images of films containing Au-PEO NPs with two different PEO ligand molecular weights, at medium areal density and after 14 h of annealing in chloroform vapor. The PEO ligands, which are highly incompatible with PS and only slightly incompatible with PMMA,[28,32] give rise to the preferential segregation of nanoparticles to PMMA domains. Short ranged, hexagonal NP packing is observed in both cases, and the nearest neighbor distance (d_1, obtained from image analysis) correlates with the molecular weight of the ligands (26.1 and 36.3 nm for the 5k and 20k ligands, respectively). For the same NP areal densities, σ, the hosting PMMA domains are more swollen when they contain Au-PEO_{20k} NPs than when they are filled with Au-PEO_{5k} NPs, due to the higher effective area occupied by the NPs in the first case. This causes a morphological change in the thickness-confined film, transforming standing lamellae (or truncated lying cylinders for this film thickness) to standing cylinders (truncated spheres). For brevity, we will refer to these two morphologies as "stripes" and "dots".

Further insight into the self-assembly process is provided by **Figure 2** and **Figure 3**, which show SEM images of PS-*b*-PMMA/Au-PEO_{5k} and PS-*b*-PMMA/Au-PEO_{20k} films for different areal densities and at several intervals during the annealing process in chloroform vapor. The insets show the radial distribution functions and average nearest neighbor distances obtained

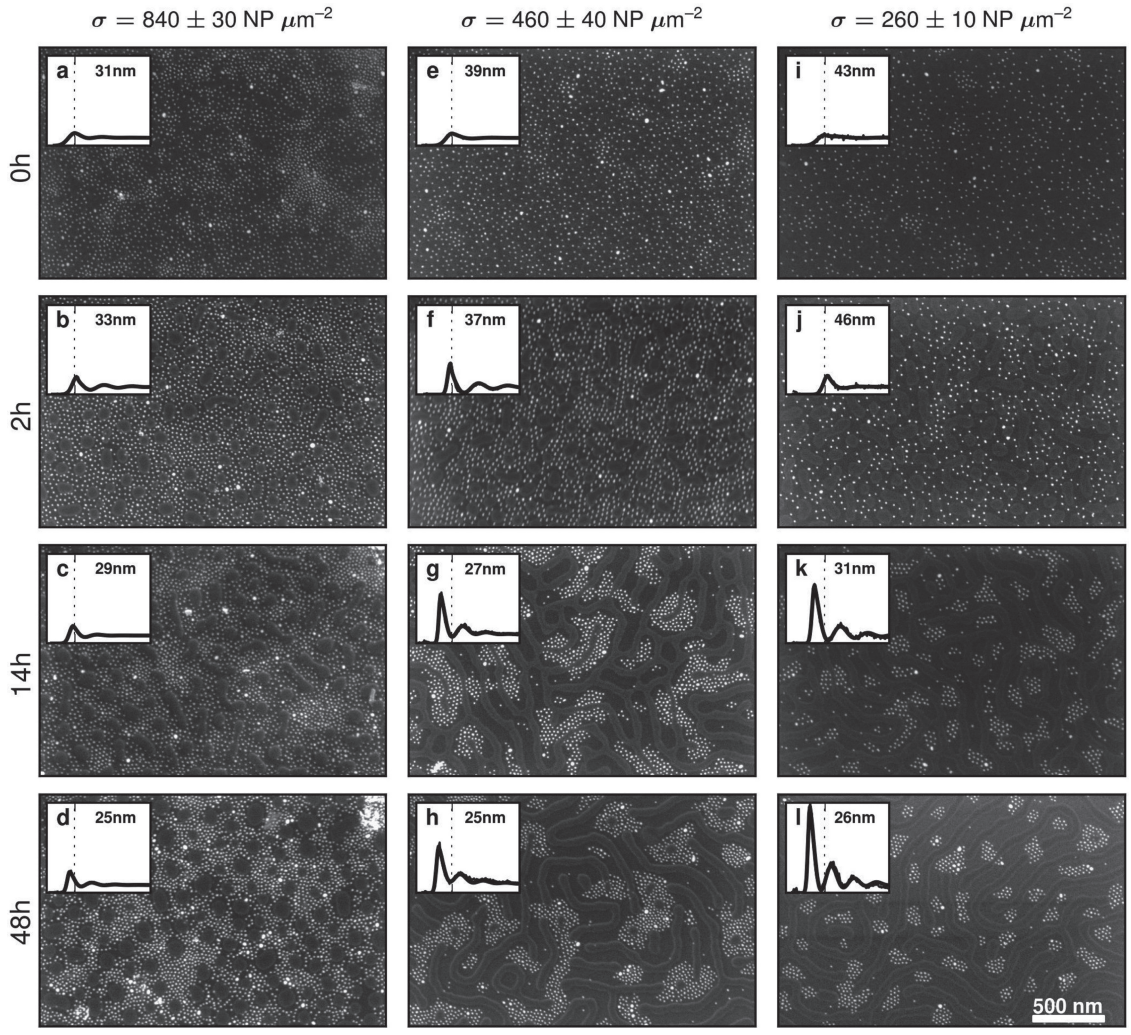

Figure 2. SEM images taken at several intervals during the annealing of PS-*b*-PMMA/Au-PEO_{5k} films with three different σ. Insets show the radial distribution functions for the nanoparticles identified in each image and corresponding fits, with a vertical line denoting the first peak position (or d_1) at 0 h. The scale bar in the lower right image (500 nm) applies to all others.

from image analysis. We shall consider the case of PS-*b*-PMMA/Au-PEO_{5k} first. Before annealing, all films show weakly phase separated PS and PMMA phases. Nanoparticles are mixed in the polymer film, distributed roughly uniformly with slight clustering that probably arises from shear stress during spin coating. After 2 h of annealing, the evolution of distinct PS and PMMA phases is observed and NPs are already located in PMMA domains. As noted above, nanoparticles swell the PMMA phase, and consequently the size and shape of the PS domains depend on the NP filling fraction. It should be noted that the nearest neighbor distance, d_1, does not change appreciably after 2 h of annealing. After 14 and 48 h of annealing, however, two major changes are observed. First, the morphology of the PS domains continues to evolve for medium and low NP filling fractions, namely the PS domains elongate and their interfaces with the PMMA domains become smoother. Second, d_1 decreases, reaching a limit of 25–27 nm after 48 h of annealing for all filling fractions. The latter observation is particularly important, since it shows that NPs tend to pack closely, a consequence of the Au-PEO nanoparticles being incompatible also with the PMMA domains. Hexagonal close packing is further corroborated by the presence of additional peaks at distinct positions in the radial distribution functions (see insets in Figure 2,3). This secondary phase separation, which succeeds the initial microphase separation of the BCP, necessarily takes place within the confines of the PMMA domains.

Analogous observations can be made for the PS-*b*-PMMA/Au-PEO_{20k} system (Figure 3). The main difference, as compared to shorter PEO-SH ligands, is an early onset of NP macrophase separation from the BCP, which is noticeable for higher filling fractions already after 14 h of annealing (Figure 3c), and after 48 h of annealing for lower filling fractions (not shown). This accelerated macrophase separation is explained by the larger size of the PEO ligands (20 kDa compared to 5 kDa), which increases the effective NP area, but more significantly, also increases the enthalpic incompatibility of the NPs with the hosting PMMA domain.

Assembling larger (19 nm) Au-PEO_{5k} NPs with shorter BCPs (M_n 243 and 100 kDa) of the same morphology, which

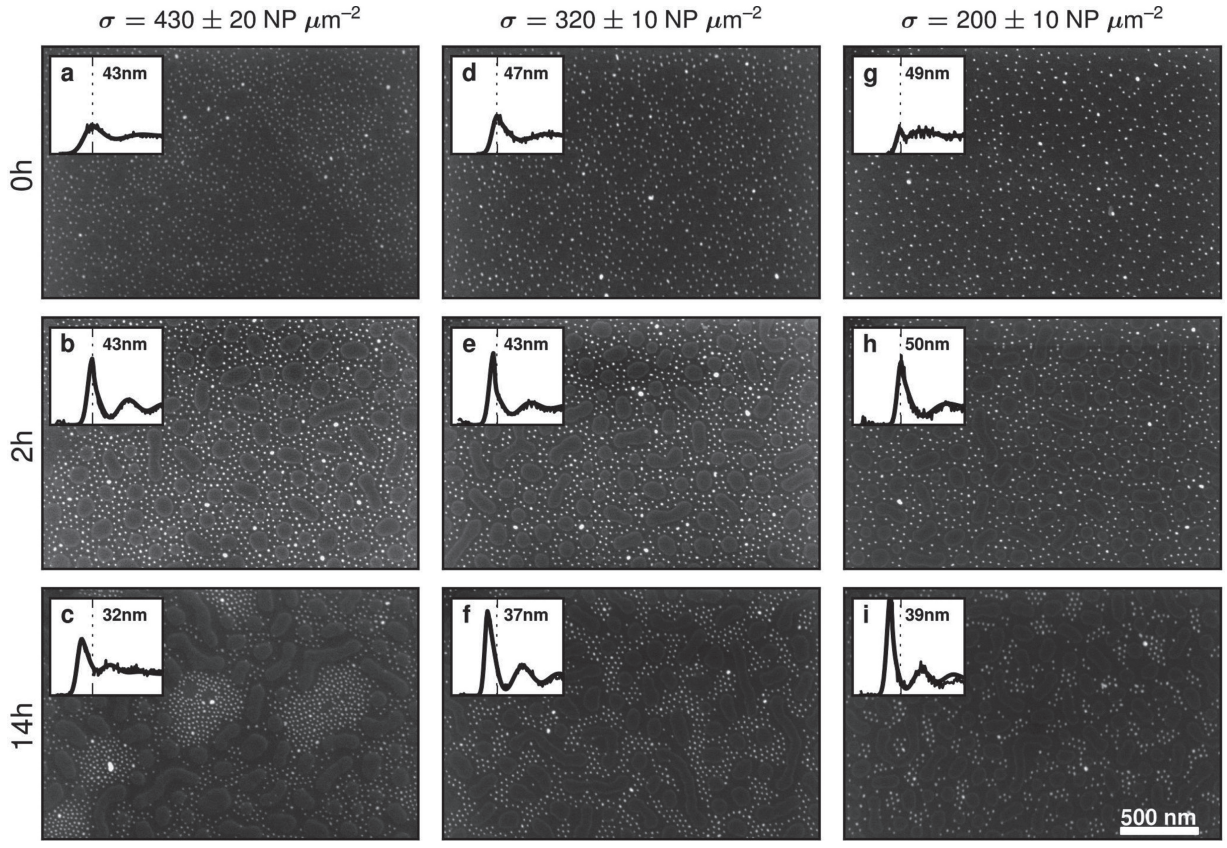

Figure 3. SEM images taken at several intervals during the annealing of PS-*b*-PMMA/Au-PEO$_{20k}$ films with three different σ. Insets show the radial distribution functions for the nanoparticles identified in each image and corresponding fits, with a vertical line denoting the first peak position (or d_1) at 0 h. The scale bar in the lower right image (500 nm) applies to all others.

display narrower PMMA domains, resulted in NP chains instead of hexagonal aggregates (see Supporting Information Figure S4). This is another manifestation of the confinement effect on the assembly. On the other hand, accelerated macrophase separation was observed in this case, despite the fact that shorter ligands and shorter BCPs should be less incompatible. As we have noted in another system,[30] this is an outcome of the starting conditions (i.e., the morphology of the as-cast film): owing to higher incompatibility, BCPs of larger molecular weights exhibit a certain degree of phase separation already in the as-cast film, thus hindering the formation of aggregates already in the initial step. The reduced concentration fluctuations of shorter BCPs in the as-cast films allows the formation of NP aggregates already upon casting, which are not broken during the microphase separation of the BCP. In such cases the BCP organizes around these aggregates.[30]

We analyzed all SEM images of appropriate quality available for each system (4.6 images per sample on average) and calculated statistics for interparticle distances. A decreasing trend in the average value of d_1 (**Figure 4**) supports our observations above based on single images (Figure 2,3).[74]

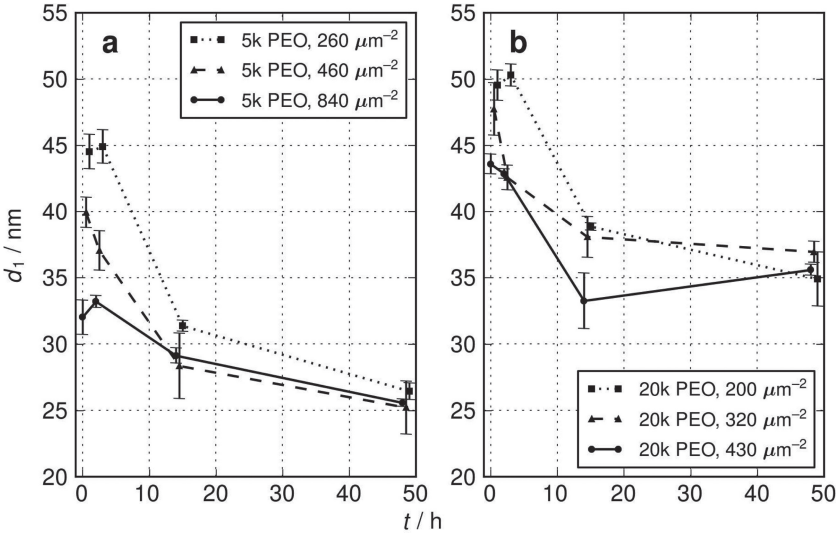

Figure 4. Evolution of d_1 (or position of the first peak in the radial distribution function) for: a) PS-*b*-PMMA/Au-PEO$_{5k}$ samples and b) PS-*b*-PMMA/Au-PEO$_{20k}$ samples. The values plotted here represent averages over all available images and the error bars correspond to the fitting error and standard deviation among images.[74]

To complement the experimental observations, we performed mesoscopic simulations using a recently developed DDFT/BD (dynamic density functional theory/Brownian dynamics) model that treats BCPs and NPs explicitly in terms of PS/PMMA-block concentration fields and NP coordinates. Molecular field theories like DDFT have been successful in unraveling a number of mechanisms underlying the phase behavior and phase transition dynamics of thin film BCP melts and solutions.[75] Our coupling of DDFT and BD is similar to recent extensions of self-consistent field theory (SCFT) that treat particles explicitly.[76] In such SCFT approaches, nanoparticles are modeled by cavities that analytically define their excluded volume in all fields. Our DDFT/BD model, on the other hand, represents them by soft particles that interact with concentration fields via a coupling free energy responsible for both excluded volume interactions and NP selectivity. Moreover, in the spirit of the original DDFT, a diffusion procedure minimizes the free energy, mimicking the dynamic experimental pathway and enabling arrest in metastable states. This is in contrast to most field-theoretic methods for nanocomposites, which focus on equilibrium behavior. One recent exception is a study by Hall et al.,[77] where a dynamic SCFT procedure is used that invokes, similar to DDFT, local instead of global equilibrium conditions, and also incorporates hydrodynamic effects for low Reynolds numbers. Here, we assume that hydrodynamic interactions are sufficiently screened after spin coating of the film, and that the BCP/NP evolution in DDFT/BD is governed by a set of coupled, purely diffusive Langevin equations. A direct comparison of diffusive DDFT with dynamic scanning force microscopy[78] has shown that all the distinct stages of a phase transition in a thin film of polystyrene-block-polybutadiene-block-polystyrene block copolymer can be correctly reproduced; a single scaling factor for structure evolution (one simulation time step ≈1 s) was even identified. In the present simulation, external potential dynamics (EPD)[79] was used for the BCP fields. The Brownian dynamics (BD) of nanoparticles, composed of multiple beads, explicitly accounts for their translational and rotational motion.

The experimental setup suggests a further decrease in the number of degrees of freedom in our model. Foremost, the perpendicular equilibrium structures in neat BCP films (see Supporting Information Figure S1) corroborate a quasi-2D conformational sampling and BCP phase separation. Additionally, the film thickness, which is comparable to the NP size, limits the NP motion in the direction normal to the substrate and effectively restricts it to the two lateral directions. Thus, simulations that are restricted to two dimensions should capture the main features of the lateral organization process. It should be noted, however, that such a restriction does not take into account terrace formation, which is generally observed in thin BCP films. However, terrace formation was not observed in our system within the selected timeframe of annealing. The restriction of the simulations to 2D also excludes scenarios involving vertical separation of the NPs from the PMMA domains (i.e., where the NPs either decorate the PMMA domains at the free surface or are segregated near the substrate, covered by the PMMA blocks). Nonetheless, such scenarios become important for the understanding of the organization only in later stages of the process, where macrophase separation of the NPs from the BCP sets in in certain cases (e.g., Figure 3c). As this study concentrates on the formation of structures with hierarchical morphologies prior to the actual macrophase separation stage, it is safe to disregard the subtleties arising from the difference between a real 2D and a quasi-2D system.

Secondly, despite the miscibility of PEO and PMMA, the disparity between the PEO ligand and PMMA block molecular weights and the grafting density (1.06 and 0.48 ligands nm^{-2} for the Au-PEO_{5k} and Au-PEO_{20k}, respectively) suggest that a PEO corona layer shields the gold core of isolated nanoparticles.[80,81] When nanoparticles start to phase separate and come into close proximity, and as the block copolymer is pushed out from between NPs, the PEO brushes reorganize to fill the interstitial spaces. For computational efficiency, we also disregard these effects and represent a grafted nanoparticle by a soft colloid with no internal degrees of freedom (see Supporting Information for details). This choice accounts for enthalpic effects, but disregards graft-related entropic contributions, which may play a role at the later stages of clustering as mentioned. The internal colloidal structure, however, can be used to tune the softness of colloids via individual coupling parameters for constituent beads. Finally, as is common practice in mesoscopic simulations, we work with monodisperse systems, both in terms of the BCP and the NPs, and include the annealing solvent only implicitly by accounting for domain swelling and screening of mean-field BCP interactions. Direct comparison to experiments will reveal to what extent these reductions in the number of degrees of freedom are realistic.

To estimate the relevant physical dimensions in simulations, we matched the final nearest neighbor distance measured (after 48 h annealing; $d_1 \approx 26$ nm in the Au-PEO_{5k} case) with the simulated one (at simulated $t = 400$ it is ≈1.7 grid points and does not change after that). Such a comparison yields a grid point resolution of 15.3 nm ± 1.5 nm, and the simulated area and nanoparticle populations were chosen accordingly. In this spirit, **Figure 5** shows the simulated evolution in a 1.3 μm^2 area with areal densities corresponding roughly to those in Figure 2 (our selection of equivalent snapshots is based on the evolution of the nearest neighbor distance). For completeness, it should be noted that the experimentally imaged area (Figure 2) is considerably larger than the area represented by the images in Figure 5.

The first observation is that our simulation predictions agree qualitatively with experiments. The microphase separation of the block copolymer proceeds relatively quickly (2 h or simulated time $t = 20$), and the average NP cluster size depends on σ. There are some small clusters and many isolated NPs for the lowest σ, and (almost) percolating network for the highest areal density. In the next stage (14 h or simulated time $t = 400$), distinct NP clusters have formed for all values of σ, with few isolated NPs left, even for the lowest areal density. For all but the highest σ, where a percolating network has already formed, the amount of NPs assembled in a cluster varies throughout the sample, although the average number per cluster is clearly larger with increasing areal density. For the highest σ, the observable mechanism is the contraction of NP clusters, providing room for the PS domains to locally coarsen into short stripes. In the final stage (48 h or simulated time $t = 1000$) the average NP cluster size has not substantially changed, but the coarsening of the BCP structure proceeds. Continuous striped

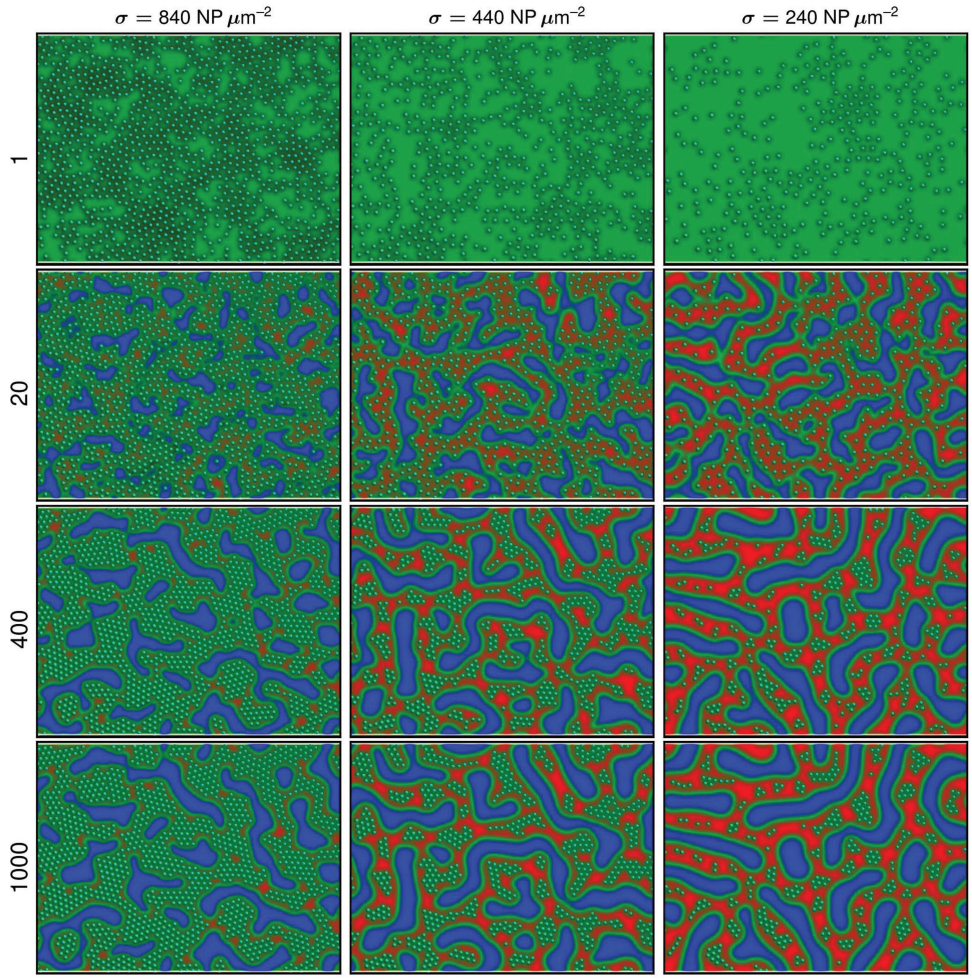

Figure 5. Selected snapshots at different simulation times for three different NP filling fractions (the simulation box represents about 1.3 μm^2). Each visible bead represents the core of a nanoparticle (shell beads not shown). The red/blue regions show respective PMMA/PS domains with order parameters above 0.90, while the green areas represent interfaces with an order parameter of 0.5.

PS domains start to form for the two lowest areal densities, σ, and grow with increasing simulation time by connecting to other PS domains. The NPs in the clusters now exhibit a minimal nearest neighbor distance d_1 and hexagonal packing (**Figure 6**). An animation of the predicted phase separation dynamics is included in the Supporting Information as a movie. **Figure 7** shows a quantitative analysis of NP ordering, in terms of d_1 and cluster size, which confirms our visual analysis, but also indicates that the structure evolution differs in details.

Analyzing the differences between the experimental and simulation results provides insights into the key factors governing the BCP/NP structure evolution. The experimental data indicate that NPs slowly sink into the BCP film during this stage (see discussion below). Moreover, the BCP chains are certainly entangled due to their high molecular weight and the presence of NPs, which act as obstacles. At later stages, the NP motion is constrained to two dimensions and the entangled BCP network adapts to avoid energetically unfavorable contacts. Overall, the nonlinear effect of entanglements on the NP evolution characteristics probably becomes less significant. Since vertical NP motion and varying entanglements are not included in our model, we cannot expect our simulations to accurately reproduce the experimental behavior during the first two hours of the annealing. The qualitative agreement of the complete structure evolution pathway, however, suggests that the fundamentals of structure formation are captured. Both in the experiments and simulations, PS domains are seen to nucleate in parts of the film where the NP fraction is the lowest. In the experiments, NPs already form a weakly ordered lattice already upon casting, which can be explained from the preparation procedure (see Supporting Information for details). Mimicking this experimental distribution in the simulations was only partly successful, and, as a result, a larger percentage of the film is almost devoid of NPs. The formation/coarsening of the PS domains thus proceeds faster compared to the experiments, and also the initial nanoparticle clustering is enhanced (Figure 7b), since the BCP structure evolution and NP dynamics are closely linked. This brief analysis explains why the structure evolution characteristics depend on the sample

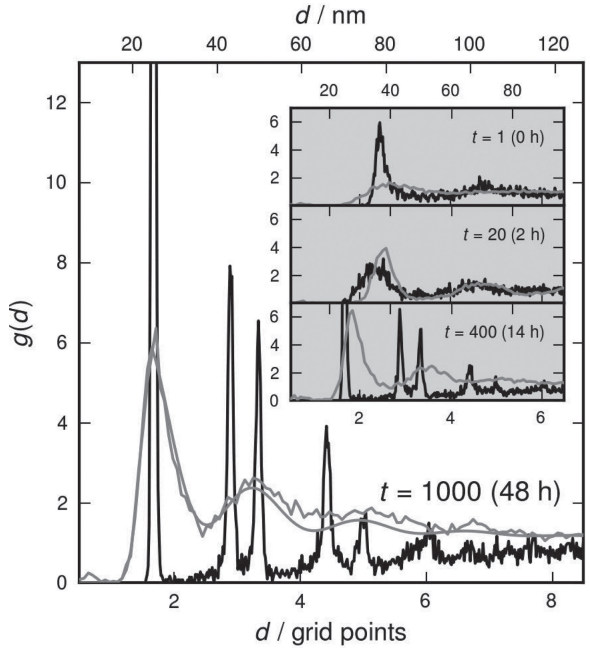

Figure 6. Comparison of radial distribution functions $g(d)$ derived from experimental images and simulations. Gray curves: PS-*b*-PMMA/Au-PEO_{5k} films after 48 h of annealing (noisy curve, corresponding to Figure 2h), with a hard sphere liquid fit (smooth line) to guide the eye. Black plot: analysis of a simulation corresponding roughly to a surface coverage of 440 NP μm^{-2} at simulated $t = 1000$ (see Figure 5). The inset shows the same types of comparisons, but for earlier experimental and simulation times.

preparation, especially on the starting NP distribution. Such an observation has also been made experimentally in other BCP/NP systems.[29,30]

The simulations identify two different mechanisms, distinguished by the NP filling fraction, for the evolution of nearest neighbor distance in Figure 7. For higher NP fractions, d_1 shifts continuously from the initial to the final (equilibrium) value, in qualitative agreement with the experimental finding. For the lowest NP fraction, however, the initial peak broadens and melts, while another peak arises near the equilibrium value and increases in magnitude with time (not shown). Insight into this effect is obtained from the potential of mean force (see Supporting Information for details), showing that the range of NP attraction is comparable to d_1 for the lowest considered NP fraction. Depending on the local BCP structure and interparticle distances, part of the NP population will thus experience a small attractive force, whereas the NPs in the remaining part first diffuse locally before experiencing attraction by other NPs, making the process diffusion-limited. Since only two experimental snapshots are available during this stage (2–14 h), we cannot confirm the second mechanism.

The difference in timescales of the microphase separation of the BCP and macrophase separation of the NPs is manifested in the tendency of NPs to separate from the interface of coarsening PS domains, which we quantify by considering the fraction of nanoparticles at the BCP interface (**Figure 8**). This effect is best observed in samples with high filling fractions. During the initial stages of phase separation, the edges of the evolving PS domains are decorated with a large number of Au-PEO NPs (Figure 8a). After prolonged annealing, however, the PS domains are surrounded by a rim devoid of NPs (Figure 8b). This evolution, which is nicely reproduced by the simulations (Figure 8c), supports our previous conclusion that the phase separation of the NPs from their hosting PMMA domains occurs on a slower timescale compared to the microphase separation of the block copolymer.

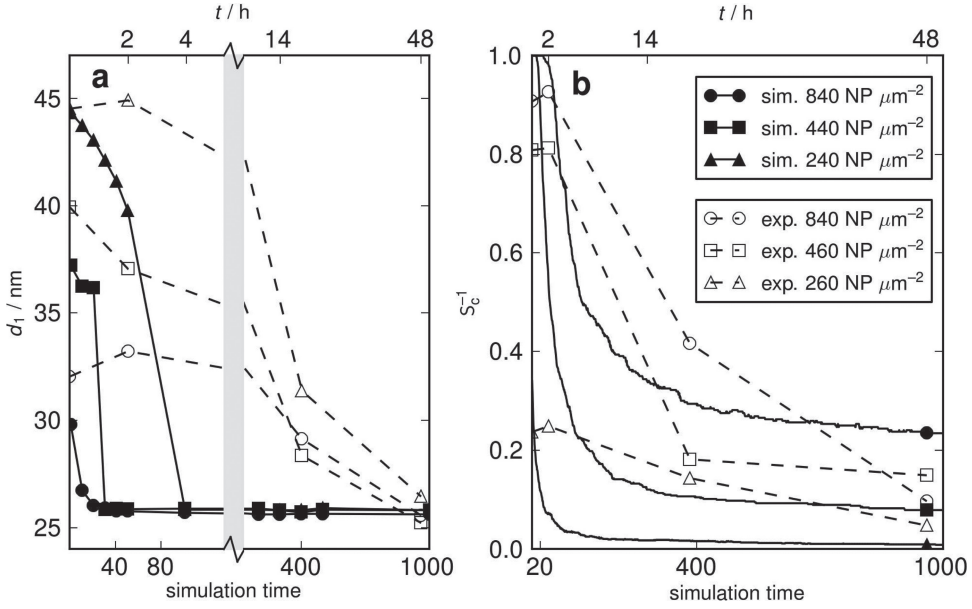

Figure 7. Evolution of: a) d_1 and b) the inverse cluster size $1/S_C$ as functions of time, with the corresponding experimental plots shown with dashed lines. Cluster sizes are plotted as inverse values in order to clearly show the transition from dispersed, predominantly isolated NPs (corresponding to $S_c = 1$) to a large percolating network ($1/S_c$ approaching 0). The axis in (a) was broken to reveal the details of the initial rapid drop in simulation values.

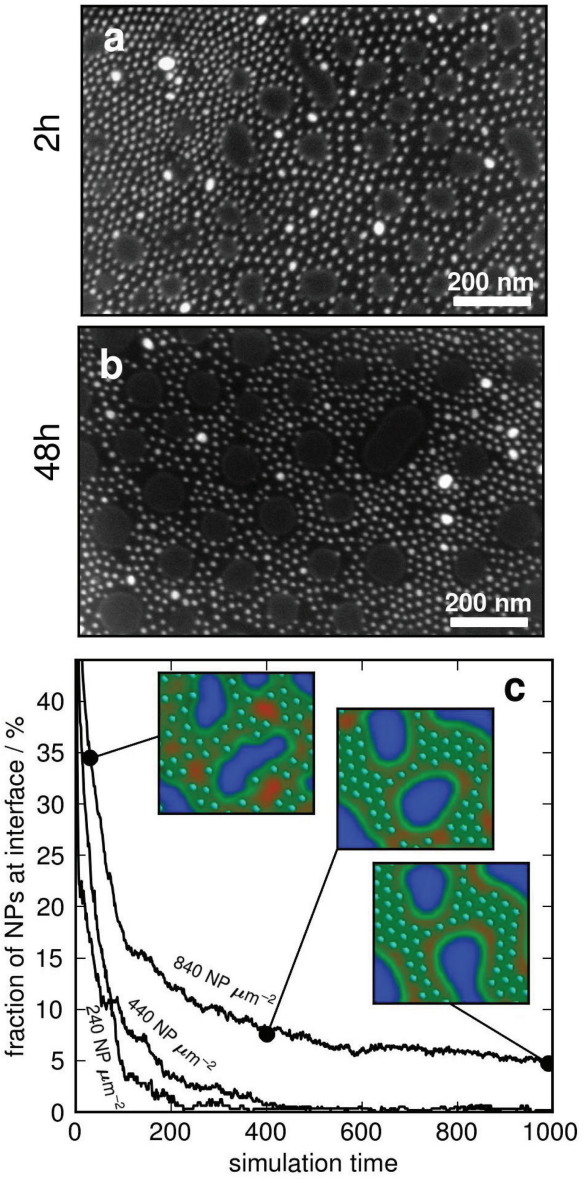

Figure 8. a,b) SEM images of a PS-*b*-PMMA/Au-PEO_{5k} film (areal density $\sigma = 1230 \pm 170$ NP µm^{-2}), demonstrating a change in the relative location of Au-PEO NPs with respect to the PS/PMMA interfaces during annealing: a) after 2 h of annealing, 31.2% NPs decorate the PS/PMMA interfaces and b) after 48 h, only 16.6% NPs remain at the PS/PMMA interfaces. c) Calculated fraction of nanoparticles at the interface during simulations, for the same three nanoparticle filling fractions presented in Figure 5. Insets show close-up views of the same region at the highest filling fraction at three representative simulation times (20, 400 and 1000).

The macrophase separation of NPs in the PS-*b*-PMMA/Au-PEO_{20k} ultrathin films deserves an additional comment, because it indicates that the hexagonal NP arrangements inside microphase separated PMMA domains are not equilibrium structures. The fact that the film thickness is on the order of the NP diameter raises questions about the mechanism by which NPs could escape the near two-dimensional confinement of PMMA domains in order to create pure NP domains. An atomic force microscopy (AFM) analysis performed on a PS-*b*-PMMA/Au-PEO_{20k} film with $\sigma = 165 \pm 20$ NP µm^{-2} after 2.5 h annealing (**Figure 9**) sheds some light on this issue. The PS domains, which are slightly softer (darker in the phase image) than the PMMA domains, protrude from the film surface, as they do in a neat copolymer film (not shown). In the PMMA phase, on the other hand, the presence of NPs seems to have caused depressions that are on average 3–4 nm deep and 30 nm wide. Nanoparticle cores can be discerned in the phase image as hard, spherical objects at the center of these dimples, surrounded by the soft (dark) PEO coronas. The mere formation of such dimples and the seeming absence of a hard gold core in many of them (for example in the top left portion of the image), suggest that the NPs sink into the PMMA matrix. Considering the polar nature of the substrate (SiO_2), the fact that PEO has a higher surface energy than either PS or PMMA at the free surface,[32] and the rather low thickness of the film, it seems plausible that the NPs are attracted to the substrate during the annealing process. Since the polar substrate may also be enriched with the PMMA phase, we speculate that such a motion toward the substrate could facilitate the ultimate macrophase separation of the NPs from the PMMA domains.

3. Conclusions

A combination of an A-B type block copolymer (PS-*b*-PMMA) with B′-type nanoparticles (Au-PEO) in thin films, where $\chi_{A,B'} >>> \chi_{A,B} \gg \chi_{B,B'}$, leads to the formation of hierarchical structures through two phase separation processes operating on different timescales. The block copolymer microphase-separates first, driven by the relatively large incompatibility between its blocks. The even larger incompatibility between the B′-NPs and the A-block causes that block to form domains where the local fraction of nanoparticles is the smallest. NPs concomitantly follow the evolution of the less incompatible domains (PMMA). The growth of the highly NP-incompatible domains (PS) can be visualized as an advancing wave that pushes the NPs with its boundary (the PS/PMMA interface). As a result, NPs decorate the interfaces in large numbers during the initial stages of phase separation. Over longer times the block copolymer phases anneal out defects, and a second, much slower phase separation process between the NPs and their hosting domains sets it. This secondary phase separation leads the NPs to depart from the A/B interfaces and to form aggregates at the centers of the hosting domains. Unlike NPs that are designed to be fully compatible with their hosting domains, in which case the NP distribution between the domains is dictated by entropic factors, the present slight incompatibility between the NPs and their hosting domains involves also enthalpic contributions. The effective attractive force between the NPs and net repulsion from the hosting domains leads to the formation of hexagonally close packed NP assemblies, where the distance between nearest neighbors is dictated by the length of the polymer chains protecting the NPs. Although these structures are not in equilibrium, the macrophase separation of the NPs from the BCP takes even longer and thus can be avoided if the annealing process is halted in time. Controlling the relative incompatibilities between the components can thus be used as a tool for

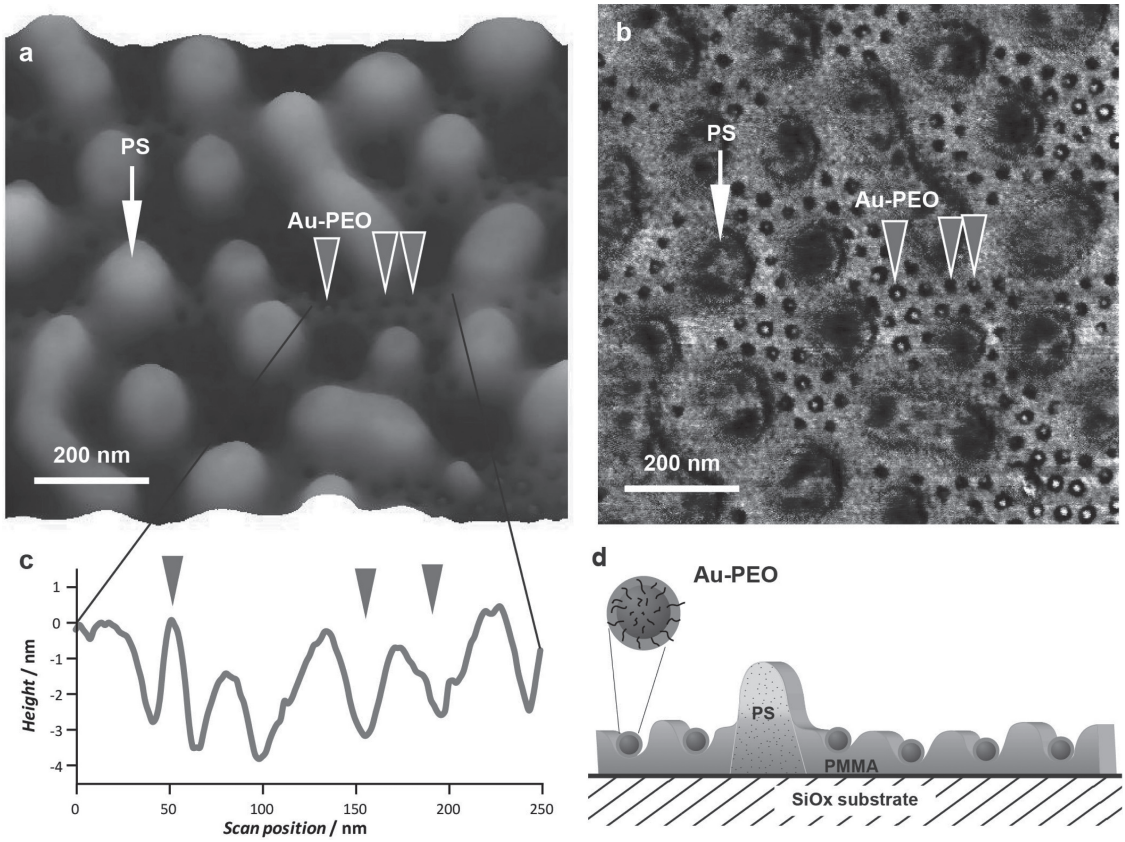

Figure 9. a) 3D surface plot of an AFM height image of a PS-*b*-PMMA/Au-PEO$_{20k}$ thin film annealed for 2.5 h ($\sigma = 165 \pm 20$ NP μm^{-2}). Higher regions appear with a lighter tone (height scale: 35 nm). The NPs create depressions (gray arrowheads) in the PMMA phase, which appears lower than the PS domains (white arrow). b) Corresponding AFM phase image (lighter tone corresponds to harder domains; vertical scale: 10°). c) Cross-section corresponding to a 250 nm line crossing the depressions in the PMMA phase caused by the NPs (line not shown for clarity). The leftmost gray arrowhead shows a NP protruding from the film depression. d) Schematic representation of the film.

obtaining more elaborate, hierarchically structured copolymer/nanoparticle assemblies.

4. Experimental Section

Materials and Synthesis: PS-*b*-PMMA (M_n 1.0 × 10^6 Da, PDI = 1.2, 35 wt% PS) was synthesized by standard anionic polymerization technique under a nitrogen atmosphere. The molecular weight, size distribution and polystyrene weight percentage were determined by gel permeation chromatography (GPC) in tetrahydrofuran (THF) against PS standards for the PS block and comparison of the ^{1}H NMR signals for phenyl and methoxy groups, respectively, for the PMMA block. Additional PS-*b*-PMMA used were either synthesized and analyzed similarly (M_n 243 kDa, PDI = 1.2, 29 wt% PS) or purchased from Polymer Source, Inc., and used as received (M_n 100 kDa, PDI = 1.1, 20 wt% PS). Polystyrene (M_n 195 kDa, PDI = 1.2) was synthesized and analyzed in a similar fashion. Poly(methyl methacrylate) (M_n 120 kDa, PDI = 2.9) was purchased from Sigma-Aldrich, and its molecular weight and size distribution were determined by GPC using universal calibration with PS standards. Tetrachloroauric acid ($HAuCl_4 \cdot 3H_2O$) was purchased from Strem Chemicals or Acros and used as received. Thiol-terminated polyethylene oxide (PEO-SH) polymers (*O*-[2-(3-Mercaptopropionylamino)ethyl]-*O′*-methylpolyethylene glycol, M_n 5 and 20 kDa), were purchased from Sigma-Aldrich and used as received.

Citrate stabilized gold nanoparticles were synthesized according to Natan's procedure.[82] Briefly, $HAuCl_4$ (40 mg) in water (100 mL) were stirred while boiling, followed by a fast addition of sodium citrate (116 mg) dissolved in water (1 mL). The solution was kept boiling for an additional 1 h, cooled to room temperature, filtered, and divided into two equal portions. To the first portion, PEO-SH 5 kDa (8 mg) was added, and to the second portion PEO-SH 20 kDa (32 mg) was added. The solutions were stirred overnight under ambient conditions. The resulting Au-PEO dispersions were transferred from the aqueous phase to chloroform using a small amount of ethanol as a co-solvent and vigorous shaking. The aqueous phase completely lost its color while the organic phase turned dark red, indicating the successful functionalization of the NPs with the PEO-SH ligands. The organic solution was washed twice with water and its volume was reduced by evaporation. To remove unreacted PEO-SH chains, the concentrated solution was centrifuged several times at 15 000 rpm for 30 min with *n*-hexane. Centrifugation was continued until no unbound PEO-SH was detected by ^{1}H NMR analysis of the supernatant. Core size distributions were determined by analysis of TEM images (see Supporting Information Table S1).

Preparation of Nanocomposite Films: Solutions containing the PS-*b*-PMMA and Au-PEO NPs were prepared by mixing a constant volume of 1 wt% copolymer solution in toluene with varying volumes of the NP chloroform solution. Chloroform was added to maintain a constant total volume and a 3:1 v/v chloroform:toluene ratio. The mixture solutions were stirred for several hours before spin coating at 3000 rpm for 30 s, onto hydrophilic silicon wafers with 120 nm thick oxide. The substrates were cleaned in a sulfuric acid-NoChromix (purchased from

Sigma-Aldrich) bath and extensively rinsed with distilled water prior to casting. The thickness of the BCP/Au-PEO films varied from 30 to 17 nm for films featuring high NP filling fractions and the neat BCP film, respectively. Samples were annealed in a closed petri dish under saturated chloroform vapor conditions for 2, 14, or 48 h. Opening the lid and removing the samples quenched the films within less than a second. A 17 nm-thick film of the neat copolymer spin-coated from 0.25 wt% toluene solution and annealed in chloroform vapor exhibits a lamellar morphology with a long period, L_0, of 150 nm, as measured by AFM (see Supporting Information Figure S1).

Characterization: GPC was performed on a Polymer Standards Service (PSS) system consisting of a PSS SDV linear M column, refractive index and UV detectors (Thermo), multiple angle light scattering (MALS) detector (BiMwA, Brookhaven), and an online viscometer (ETA 2010, WGE Dr. Bures). Data analysis and universal calibration (with PS standards) were performed using PSS WinGPC software. The size of the polymer-coated gold nanoparticles was determined by transmission electron microscopy (TEM) using a Tecnai T12 G2 Spirit microscope operated at 120 kV. The gold core diameter distribution, obtained as a histogram from TEM image analysis, was used to calculate the average surface area per gold nanoparticle. The average number of chains per particle and the chain density on the surface of the particles were calculated from ligand weight fractions determined by TGA (performed on a Mettler-Toledo TGA/DSC 1 analyzer, measuring weight loss under nitrogen flow between 50–600 °C at a heating rate of 10 °C min^{-1}). Dynamic light scattering (DLS) and zeta potential measurements were performed on a Nano-ZS Zetasizer (Malvern UK) in chloroform and water, respectively, and showed an increase in the hydrodynamic radii and a decrease in the NP surface charge compared to the citrate stabilized Au nanoparticles. Supporting Information, Table S1, summarizes all the relevant NP characteristics.

HR-SEM images of the PS-*b*-PMMA/Au-PEO films were acquired with a Sirion microscope (FEI Company) at 5 or 10 kV acceleration voltages. AFM images were recorded on a Dimension 3100 scanning probe microscope with a Nanoscope V controller, Veeco, Santa-Barbara, USA.

Image Analysis: NP areal densities and the average d_1 were calculated from 2–10 images (average of 4.6 images) for each sample as follows. The images were processed (Gaussian filtering, adjusting brightness and contrast), thresholded and segmented into individual nanoparticles (see Supporting Information for details). Segmentation was performed by identifying regional maxima in the intensity and watersheding (with a flooding algorithm) the thresholded image using these regional maxima as seeds. Radial distribution functions based on these segmented images (as shown in Figure 2,3,6) were normalized and corrected for edge effects, and fitted with an analytical approximation for hard sphere liquids.[83] Clustering analysis was also performed (Figure 7 shows the inverse average cluster size) using the density-based DBSCAN algorithm as implemented in scikits-learn,[84] with a maximum distance of 32 nm between any two neighboring NPs in the same cluster. The entire image analysis procedure was automated with scripts,[85] and the resulting segmentation was checked visually for errors, parameters being tuned in many cases to achieve the desired segmentation quality.

Simulations: The evolution of structure in the experimental samples was simulated using a new DDFT/BD description that treats both the BCP and NPs explicitly, recently reviewed along with other methods.[76] All parameters used in the simulation are expressed in dimensionless units; where physical dimension are given above, values were obtained by matching the final average nearest neighbor distance as observed in experimental images and extracted from simulations. A simulation volume of $86 \times 64 \times 1$ (in dimensionless field grid points) was always used, with periodic boundary conditions in each direction. Several slightly larger and smaller grids were tested, with no systematic effect on the results. Below we shortly summarize our choice of parameters, and the reader is referred to the Supporting Information and relevant references for details.

We selected a coarse-grained molecular chain representation of $A_{16}B_{20}$ (each bead represents roughly 300 monomers) for the BCP (A and B denote PS and PMMA, respectively), based on the experimental volume ratio PS:PMMA = 3:5 and comparison with the phase behavior of neat PS-*b*-PMMA films. In previous single-chain in mean field (SCMF) and Monte Carlo (MC) studies of experimental thin PS-*b*-PMMA films containing NPs, a range of $\chi_{AB}N$ values have been considered, including 20,[86] 25,[87] 37,[88] and 63.2[70] without much discussion. In contrast to our experimental setup (dried films are annealed in chloroform vapor at room temperature), these studies used toluene for film preparation and annealing in vacuum at elevated temperatures (190–230 °C). It is well known that the Flory-Huggins $\chi_{PS\text{-}PMMA}$ parameter varies only weakly with temperature,[89] and we need to account for solvent screening during annealing. Considering that a significantly reduced time step is required for higher χ_{AB} N values, we chose χ_{AB} $N = 24$ as a reasonable value for this system.

NPs were represented by tightly-bound, stiff clusters of core and shell beads. Each constituent bead carries a set of coupling parameters that define its interactions with all concentration fields (in our case, BCP blocks) present in the system. The core bead will typically carry significantly higher coupling parameters than shell beads (around 10–15 compared to 1-2), but only shell beads (representing PEO ligands) are selective towards one block. A model with explicit PEO ligands is feasible, but the simplicity of this colloid representation makes choosing parameters (notoriously difficult in any mesoscopic model) considerably easier. We tested a range of coupling parameters for our model, and the results presented here are for a core bead coupling parameter of 10, and shell bead coupling parameters of 1.0 (with the PMMA block) and 1.5 (with the PS block). There is also a short-ranged DPD-like repulsion between all beads that accounts for the "softness" of the PEO shell and determines the final nearest neighbor distance (in the presented simulations $a_{pp} = 10$).

In contrast to SCFT, DDFT deals with slightly compressible systems, and penalizes pressure variations through a Helfand compressibility term. The associated Helfand parameter κ_H and the particle—field coupling parameters described above cannot be chosen independently. Matching the isothermal compressibility of water provides $\kappa_H = 15$, and this is the value we used.

The evolution of the model is described by Langevin dynamics with alternating particle Brownian moves (translation and rotation with a common diffusion coefficient) and field updates, and a constant time step $\Delta t = 0.01$ (simulation time is therefore $t = n\Delta t$, where n is the number of time steps). Density fields for BCP blocks are updated using EPD[79] and a discrete Crank-Nicolson scheme.[90] The model for collective dynamics in EPD accounts for BCP chain connectivity at the Rouse level, as well as for reptation in homogeneous homopolymer melts provided the Rouse diffusion coefficient is appropriately scaled (the models are thus equivalent in dimensionless units). Following standard DDFT practice, the reduction in the number of degrees of freedom is reflected in the noise amplitude ($\Omega = 100$); similarly, the NP size in BD is accounted for by a noise scaling factor $T^* = 0.01$. The ratio between field and particle diffusion coefficients, D_f/D_p, sets the rate at which the competing phase separations (between BCP blocks and between the BCP and NPs) take place. Guided by a comparison with the experimental system, we consider $D_f > D_p$, and set $D_p = 0.01$ and $D_f = 1.0$.

Supporting Information

Supporting Information is available from the Wiley Online Library or from the author.

Acknowledgements

This research was supported by a NanoSci-E+ grant (MEMORY project) and the Israel Science Foundation (grant number 562/10).

Received: January 9, 2013
Revised: February 9, 2013
Published online: March 27, 2013

[1] N. Krasteva, I. Besnard, B. Guse, R. E. Bauer, K. Müllen, A. Yasuda, T. Vossmeyer, *Nano Lett.* **2002**, *2*, 551.
[2] M. P. Pileni, *Acc. Chem. Res.* **2007**, *40*, 685.
[3] I. Lisiecki, D. Parker, C. Salzemann, M. P. Pileni, *Chem. Mater.* **2007**, *19*, 4030.
[4] B. L. Frankamp, A. K. Boal, M. T. Tuominen, V. M. Rotello, *J. Am. Chem. Soc.* **2005**, *127*, 9731.
[5] S. Srivastava, B. L. Frankamp, V. M. Rotello, *Chem. Mater.* **2005**, *17*, 487.
[6] B. Nikoobakht, Z. L. Wang, M. A. El-Sayed, *J. Phys. Chem. B* **2000**, *104*, 8635.
[7] K. G. Thomas, S. Barazzouk, B. I. Ipe, S. T. S. Joseph, P. V. Kamat, *J. Phys. Chem. B* **2004**, *108*, 13066.
[8] Z. H. Nie, D. Fava, M. Rubinstein, E. Kumacheva, *J. Am. Chem. Soc.* **2008**, *130*, 3683.
[9] Z. H. Nie, D. Fava, E. Kumacheva, S. Zou, G. C. Walker, M. Rubinstein, *Nat. Mater.* **2007**, *6*, 609.
[10] M. R. Bockstaller, E. L. Thomas, *Phys. Rev. Lett.* **2004**, *93*, 166106.
[11] P. A. Mistark, S. Park, S. E. Yalcin, D. H. Lee, O. Yavuzcetin, M. T. Tuominen, T. P. Russell, M. Achermann, *ACS Nano* **2009**, *3*, 3987.
[12] M. R. Bockstaller, R. A. Mickiewicz, E. L. Thomas, *Adv. Mater.* **2005**, *17*, 1331.
[13] A. Haryono, W. H. Binder, *Small* **2006**, *2*, 600.
[14] M. J. Pavan, R. Shenhar, *J. Mater. Chem.* **2011**, *21*, 2028.
[15] S. C. Warren, L. C. Messina, L. S. Slaughter, M. Kamperman, Q. Zhou, S. M. Gruner, F. J. DiSalvo, U. Wiesner, *Science* **2008**, *320*, 1748.
[16] J. J. Chiu, B. J. Kim, E. J. Kramer, D. J. Pine, *J. Am. Chem. Soc.* **2005**, *127*, 5036.
[17] E. Reister, G. H. Fredrickson, *J. Chem. Phys.* **2005**, *123*, 214903.
[18] B. J. Kim, J. Bang, C. J. Hawker, E. J. Kramer, *Macromolecules* **2006**, *39*, 4108.
[19] B. J. Kim, G. H. Fredrickson, E. J. Kramer, *Macromolecules* **2008**, *41*, 436.
[20] K. Tsutsumi, Y. Funaki, Y. Hirokawa, T. Hashimoto, *Langmuir* **1999**, *15*, 5200.
[21] C. M. Huang, K. H. Wei, U. S. Jeng, K. S. Liang, *Macromolecules* **2007**, *40*, 5067.
[22] S. Zou, R. Hong, T. Emrick, G. C. Walker, *Langmuir* **2007**, *23*, 1612.
[23] Q. F. Li, J. B. He, E. Glogowski, X. F. Li, J. Wang, T. Emrick, T. P. Russell, *Adv. Mater.* **2008**, *20*, 1462.
[24] P. J. Costanzo, F. L. Beyer, *Macromolecules* **2007**, *40*, 3996.
[25] M. W. Matsen, R. B. Thompson, *Macromolecules* **2008**, *41*, 1853.
[26] C. Xu, K. Ohno, V. Ladmiral, R. J. Composto, *Polymer* **2008**, *49*, 3568.
[27] C. Xu, K. Ohno, V. Ladmiral, D. E. Milkie, J. M. Kikkawa, R. J. Composto, *Macromolecules* **2009**, *42*, 1219.
[28] R. D. Deshmukh, Y. Liu, R. J. Composto, *Nano Lett.* **2007**, *7*, 3662.
[29] E. Ploshnik, A. Salant, U. Banin, R. Shenhar, *Adv. Mater.* **2010**, *22*, 2774.
[30] E. Ploshnik, A. Salant, U. Banin, R. Shenhar, *Phys. Chem. Chem. Phys.* **2010**, *12*, 11885.
[31] B. J. Kim, J. J. Chiu, G. R. Yi, D. J. Pine, E. J. Kramer, *Adv. Mater.* **2005**, *17*, 2618.
[32] S. C. Park, B. J. Kim, C. J. Hawker, E. J. Kramer, J. Bang, J. S. Ha, *Macromolecules* **2007**, *40*, 8119.
[33] B. J. Kim, G. H. Fredrickson, J. Bang, C. J. Hawker, E. J. Kramer, *Macromolecules* **2009**, *42*, 6193.
[34] Y. Lin, A. Böker, J. B. He, K. Sill, H. Q. Xiang, C. Abetz, X. F. Li, J. Wang, T. Emrick, S. Long, Q. Wang, A. Balazs, T. P. Russell, *Nature* **2005**, *434*, 55.
[35] J. B. He, R. Tangirala, T. Emrick, T. P. Russell, A. Böker, X. F. Li, J. Wang, *Adv. Mater.* **2007**, *19*, 381.
[36] S. W. Yeh, K. H. Wei, Y. S. Sun, U. S. Jeng, K. S. Liang, *Macromolecules* **2003**, *36*, 7903.
[37] U. S. Jeng, Y. S. Sun, H. Y. Lee, C. H. Hsu, K. S. Liang, S. W. Yeh, K. H. Wei, *Macromolecules* **2004**, *37*, 4617.
[38] Y. S. Sun, U. S. Jeng, K. S. Liang, S. W. Yeh, K. H. Wei, *Polymer* **2006**, *47*, 1101.
[39] S. W. Yeh, K. H. Wei, Y. S. Sun, U. S. Jeng, K. S. Liang, *Macromolecules* **2005**, *38*, 6559.
[40] M. J. Park, K. Char, J. Park, T. Hyeon, *Langmuir* **2006**, *22*, 1375.
[41] C. T. Lo, C. J. Chao, *Langmuir* **2009**, *25*, 12865.
[42] M. K. Gaines, S. D. Smith, J. Samseth, M. R. Bockstaller, R. B. Thompson, K. O. Rasmussen, R. J. Spontak, *Soft Matter* **2008**, *4*, 1609.
[43] V. Pryamitsyn, V. Ganesan, *Macromolecules* **2006**, *39*, 8499.
[44] B. Lee, C.-T. Lo, S. Seifert, N. L. D. Rago, R. E. Winans, P. Thiyagarajan, *Macromolecules* **2007**, *40*, 4235.
[45] C.-T. Lo, B. Lee, V. G. Pol, N. L. D. Rago, S. Seifert, R. E. Winans, P. Thiyagarajan, *Macromolecules* **2007**, *40*, 8302.
[46] C.-T. Lo, B. Lee, N. L. D. Rago, R. E. Winans, P. Thiyagarajan, *Macromol. Rapid Commun.* **2007**, *28*, 1607.
[47] F. Reis, *Macromolecules* **2008**, *41*, 8932.
[48] L. He, L. Zhang, H. Liang, *J. Phys. Chem. B* **2008**, *112*, 4194.
[49] M. M. A. Kashem, J. Perlich, A. Diethert, W. N. Wang, M. Memesa, J. S. Gutmann, E. Majkova, I. Capek, S. V. Roth, W. Petry, P. Müller-Buschbaum, *Macromolecules* **2009**, *42*, 6202.
[50] B. Hamdoun, D. Ausserré, V. Cabuil, S. Joly, *J. Phys. II* **1996**, *6*, 503.
[51] B. Hamdoun, D. Ausserré, S. Joly, *J. Phys. II* **1996**, *6*, 1207.
[52] S. G. Jang, B. J. Kim, C. J. Hawker, E. J. Kramer, *Macromolecules* **2011**, *44*, 9366.
[53] S. G. Jang, A. Khan, M. D. Dimitriou, B. J. Kim, N. A. Lynd, E. J. Kramer, C. J. Hawker, *Soft Matter* **2011**, *7*, 6255.
[54] B. J. Kim, G. H. Fredrickson, C. J. Hawker, E. J. Kramer, *Langmuir* **2007**, *23*, 7804.
[55] B. Hamdoun, D. Ausserré, S. Joly, Y. Gallot, V. Cabuil, C. Clinard, *J. Phys. II* **1996**, *6*, 493.
[56] V. Lauter-Pasyuk, H. J. Lauter, D. Ausserré, Y. Gallot, V. Cabuil, E. I. Kornilov, B. Hamdoun, *Physica B* **1998**, *241–243*, 1092.
[57] V. Lauter-Pasyuk, H. J. Lauter, D. Ausserré, Y. Gallot, V. Cabuil, B. Hamdoun, E. I. Kornilov, *Physica B* **1998**, *248*, 243.
[58] M. R. Bockstaller, Y. Lapetnikov, S. Margel, E. L. Thomas, *J. Am. Chem. Soc.* **2003**, *125*, 5276.
[59] J. J. Chiu, B. J. Kim, G. R. Yi, J. Bang, E. J. Kramer, D. J. Pine, *Macromolecules* **2007**, *40*, 3361.
[60] M. R. Bockstaller, H. J. Ryu, S. Ojha, J. Choi, *J. Mater. Chem.* **2010**, *20*, 9339.
[61] J. Huh, V. V. Ginzburg, A. C. Balazs, *Macromolecules* **2000**, *33*, 8085.
[62] R. B. Thompson, V. V. Ginzburg, M. W. Matsen, A. C. Balazs, *Science* **2001**, *292*, 2469.
[63] J. Y. Lee, R. B. Thompson, D. Jasnow, A. C. Balazs, *Phys. Rev. Lett.* **2002**, *89*, 155503.
[64] J. Y. Lee, R. B. Thompson, D. Jasnow, A. C. Balazs, *Macromolecules* **2002**, *35*, 4855.
[65] J. H. Jin, J. Z. Wu, *J. Chem. Phys.* **2008**, *128*, 074901.
[66] H. Hasegawa, T. Hashimoto, *Macromolecules* **1985**, *18*, 589.
[67] E. Huang, L. Rockford, T. P. Russell, C. J. Hawker, *Nature* **1998**, *395*, 757.
[68] M. J. Fasolka, A. M. Mayes, *Annu. Rev. Mater. Res.* **2001**, *31*, 323.
[69] T. Xu, C. J. Hawker, T. P. Russell, *Macromolecules* **2005**, *38*, 2802.
[70] H. Kang, F. A. Detcheverry, A. N. Mangham, M. P. Stoykovich, K. C. Daoulas, R. J. Hamers, M. Müller, J. J. de Pablo, P. F. Nealey, *Phys. Rev. Lett.* **2008**, *100*, 148303.
[71] $\chi_{PS,PMMA} = 0.04$ (see T. P. Russell, R. P. Hjelm, P. A. Seeger, *Macromolecules* **1990**, *23*, 890) and $\chi_{PS,PEO} = 0.28$ (see M. Nagata, T. Fukuda, H. Inagaki, *Macromolecules* **1987**, *20*, 2173–2178). The experimentally determined value of $\chi_{PMMA,PEO}$ in blends is slightly

negative, and diminishes for increasing PMMA volume fraction (see H. Ito, T. P. Russell, G. D. Wignall, *Macromolecules* **1987**, *20*, 2213–2220). In our system, where the PEO ligands are immobilized on the NP surface, the NPs are clearly immiscible with PMMA (see Supporting Information Figure S2). This is explained by the fact that the PMMA blocks are very long compared to the PEO ligands, thus should be effectively excluded from the PEO brush (i.e., the PMMA matrix is incompatible with the PEO-protected gold NPs). Nonetheless, it is expected that the incompatibility between the Au-PEO NPs and the PMMA blocks would have a lower χ value than $\chi_{PS,PMMA}$, as also demonstrated by the faster microphase separation of the BCP.

[72] The annealing solvent should also be taken into account within the thermodynamic considerations. However, chloroform is the closest to a non-selective solvent for the three polymers involved. Additionally, it is expected that the low concentration of chloroform vapour in the film will not change the order of the pairwise interaction parameters mentioned in the previous note.

[73] The assembly of PS-*b*-PMMA with Au-PEO NPs has been investigated by others, but they concentrated on different aspects: Kramer and coworkers[32] focused on how NPs and preparation conditions affect the ordering of BCP domains, using a more complex annealing procedure and a much shorter BCP with a minority PMMA block; Composto et al.[28] described the two dimensional confinement of Au-PEO nanorods in lamellar PS-*b*-PMMA.

[74] The relatively large error bars in the case of PS-*b*-PMMA/Au-PEO_{5k} with areal density 450 NP μm^{-2} originates from the fact that the analysis of this system included images obtained from two different samples, which were prepared under analogous conditions. Thus, the error bars in this case provide an estimate of sample variation due to preparation conditions, which is not too high (5 nm compared to 1–2 nm for single samples), and does not disturb the main trend observed here.

[75] L. Tsarkova, G. J. A. Sevink, G. Krausch, in *Complex Macromolecular Systems I*, Vol. *227* (Ed: A. H. E. Müller, H. W. Schmidt), Springer-Verlag, Berlin **2010**, p. 33–73.

[76] K. M. Langner, G. J. A. Sevink, *Soft Matter* **2012**, *8*, 5102.

[77] D. M. Hall, T. Lookman, S. Banerjee, *Chem. Eng. Sci.* **2009**, *64*, 4754.

[78] A. Knoll, K. S. Lyakhova, A. Horvat, G. Krausch, G. J. A. Sevink, A. V. Zvelindovsky, R. Magerle, *Nat. Mater.* **2004**, *3*, 886.

[79] N. M. Maurits, J. Fraaije, *J. Chem. Phys.* **1997**, *107*, 5879.

[80] F. S. Bates, G. H. Fredrickson, *Macromolecules* **1994**, *27*, 1065.

[81] L. Yezek, W. Schärtl, Y. M. Chen, K. Gohr, M. Schmidt, *Macromolecules* **2003**, *36*, 4226.

[82] K. C. Grabar, R. G. Freeman, M. B. Hommer, M. J. Natan, *Anal. Chem.* **1995**, *67*, 735.

[83] E. Matteoli, G. A. Mansoori, *J. Chem. Phys.* **1995**, *103*, 4672.

[84] F. Pedregosa, G. Varoquaux, A. Gramfort, V. Michel, B. Thirion, O. Grisel, M. Blondel, P. Prettenhofer, R. Weiss, V. Dubourg, J. Vanderplas, A. Passos, D. Cournapeau, M. Brucher, M. Perrot, E. Duchesnay, *J. Mach. Learn. Res.* **2011**, *12*, 2825.

[85] Python scripts performing simulations and image analysis are available at http://github.com/langner/memory-task0013. Simulation scripts wrap the Culgi simulation package (www.culgi.com), and image analysis scripts are based on the pymorph and mahotas modules (available at http://github.com/luispedro). Results presented here use code revisions from July 2012.

[86] M. Yoo, S. Kim, S. G. Jang, S.-H. Choi, H. Yang, E. J. Kramer, W. B. Lee, B. J. Kim, J. Bang, *Macromolecules* **2011**, *44*, 9356.

[87] U. Nagpal, H. Kang, G. S. W. Craig, P. F. Nealey, J. J. de Pablo, *ACS Nano* **2011**, *5*, 5673.

[88] E. W. Edwards, M. Müller, M. P. Stoykovich, H. H. Solak, J. J. de Pablo, P. F. Nealey, *Macromolecules* **2007**, *40*, 90.

[89] P. F. Green, T. P. Russell, R. Jerome, M. Granville, *Macromolecules* **1988**, *21*, 3266.

[90] B. A. C. van Vlimmeren, N. M. Maurits, A. V. Zvelindovsky, G. J. A. Sevink, J. Fraaije, *Macromolecules* **1999**, *32*, 646.